Electronic Supplementary Information

Contact Electrification Between Identical Polymers as the Basis for Triboelectric/Flexoelectric Materials

Andris Šutka,*[a] Kaspars Mālnieks,[a] Linards Lapčinskis,[b] Martin Timusk,[c] Kaspars Kalniņš,[d] Andrejs Kovaļovs,[d] Juris Bitenieks,[e] Māris Knite,[b] Daniel Stevens,[f] Jaime Grunlan *[g]

Affiliations:

a. Research Laboratory of Functional Materials Technologies, Faculty of Materials Science and Applied Chemistry, Riga Technical University, Paula Valdena 3/7, 1048 Riga, Latvia

Corresponding author e-mail: Andris.Sutka@rtu.lv

b. Institute of Technical Physics, Faculty of Materials Science and Applied Chemistry, Riga Technical University, Paula Valdena 3/7, 1048 Riga, Latvia

c. Institute of Physics, University of Tartu, W. Ostwaldi Str. 1, 50411 Tartu, Estonia

d. Institute of Materials and Structures, Faculty of Civil Engineering, Riga Technical University, Kipsalas 6A, 1048 Riga, Latvia

e. Institute of Polymer Materials, Faculty of Materials Science and Applied Chemistry, Riga Technical University, Paula Valdena 3/7, 1048 Riga, Latvia

f. Department of Chemistry, Texas A&M University, College Station, TX 77843, USA

g. Departments of Mechanical Engineering, Materials Science and Engineering, and Chemistry, Texas A&M University, College Station, TX 77843, USA

Corresponding author e-mail: jgrunlan@tamu.edu

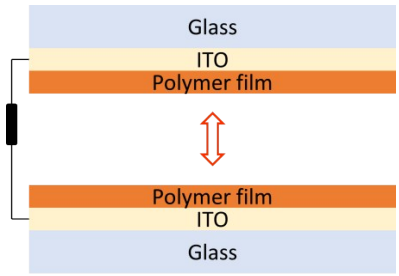

Figure S1. Schematic of a triboelectric nanogenerator (TENG) device. Surface charge formed on the polymer induces electrostatic charge on the electrode plates. Upon oscillation, the potential between the two plates is changed and electron flow occurs to balance this potential change.

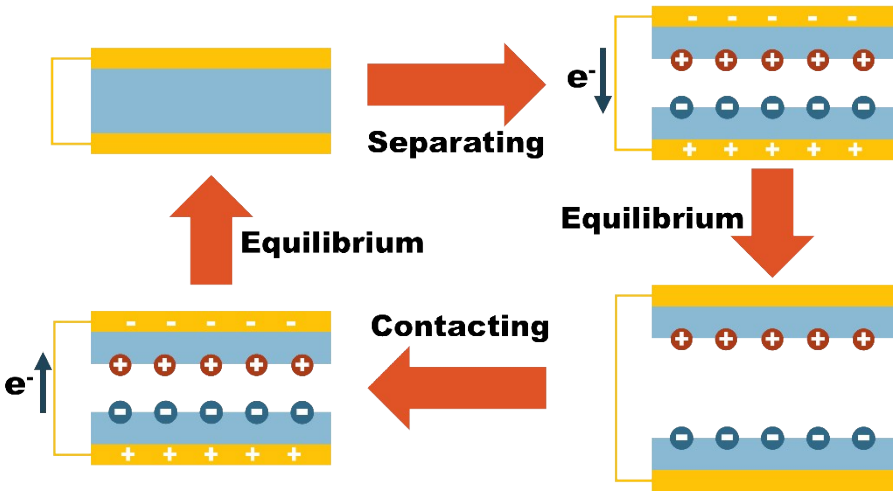

Figure S2. Schematic representation of TENG device working principle.

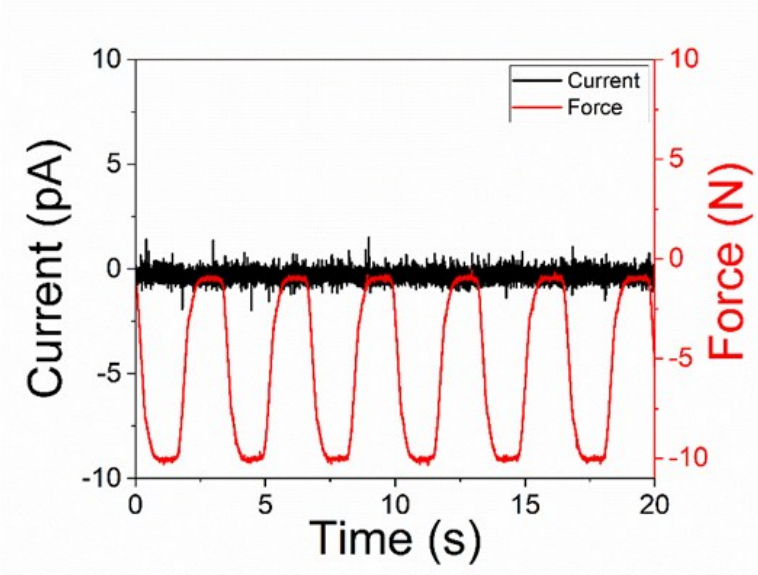

Figure S3. Short circuit current *(I_{SC})* measured from PVDF films in the piezo-regime.

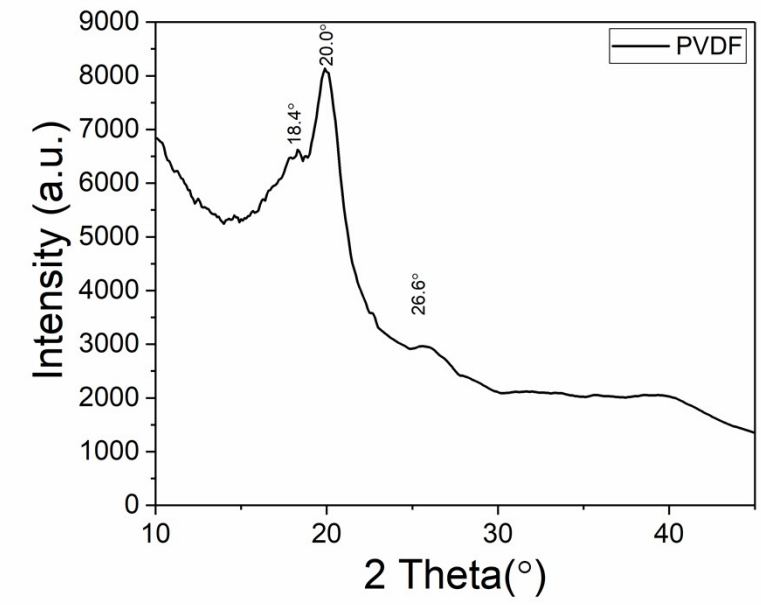

Figure S4. XRD pattern of PVDF film precipitated from 15 wt% dimethylformamide solution in methanol non-solvent that exhibits only the α phase, as evidenced by the two strong diffraction peaks at 18.4 and 20.0° and a medium peak at 26.6°, corresponding to 020, 110 and 021 reflections of the monoclinic α-phase crystal, respectively (ICCD standard card 00-042-1650).

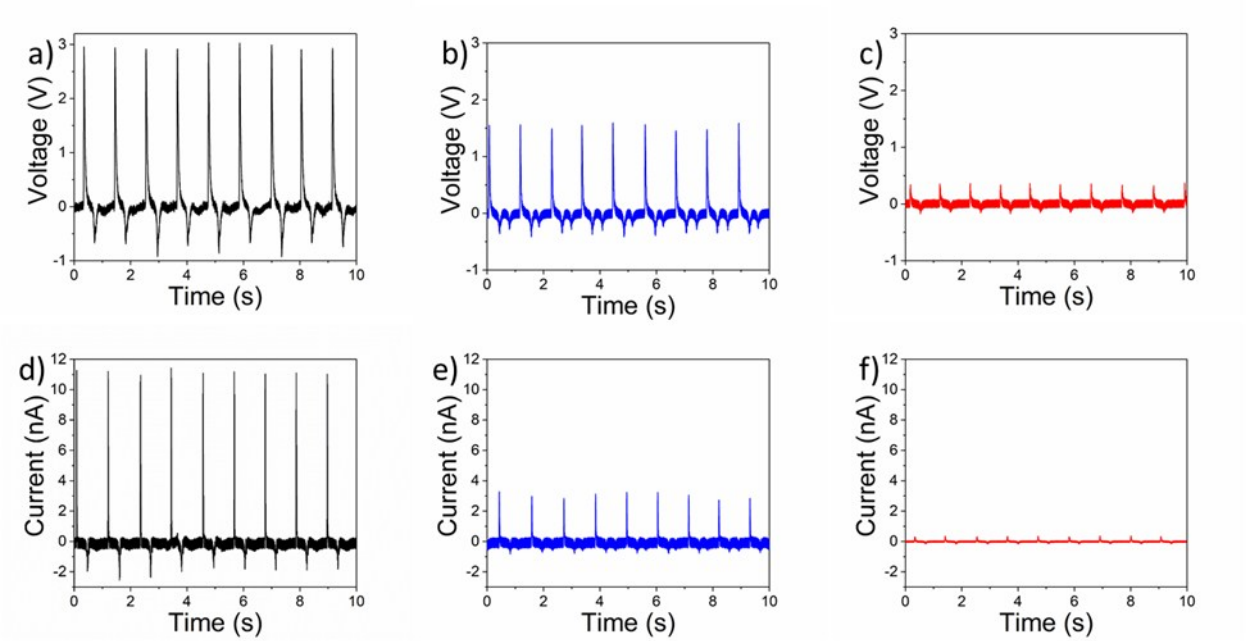

Figure S5. Open-circuit voltage (V_{OC}) generated by the TENG device based on EC: (a) smooth vs porous films, (b) porous vs porous films, (c) smooth vs smooth films. Short-circuit current (I_{SC}) generated by the EC-based TENG device: (d) smooth vs porous films, (e) porous vs porous films, (f) smooth vs smooth.

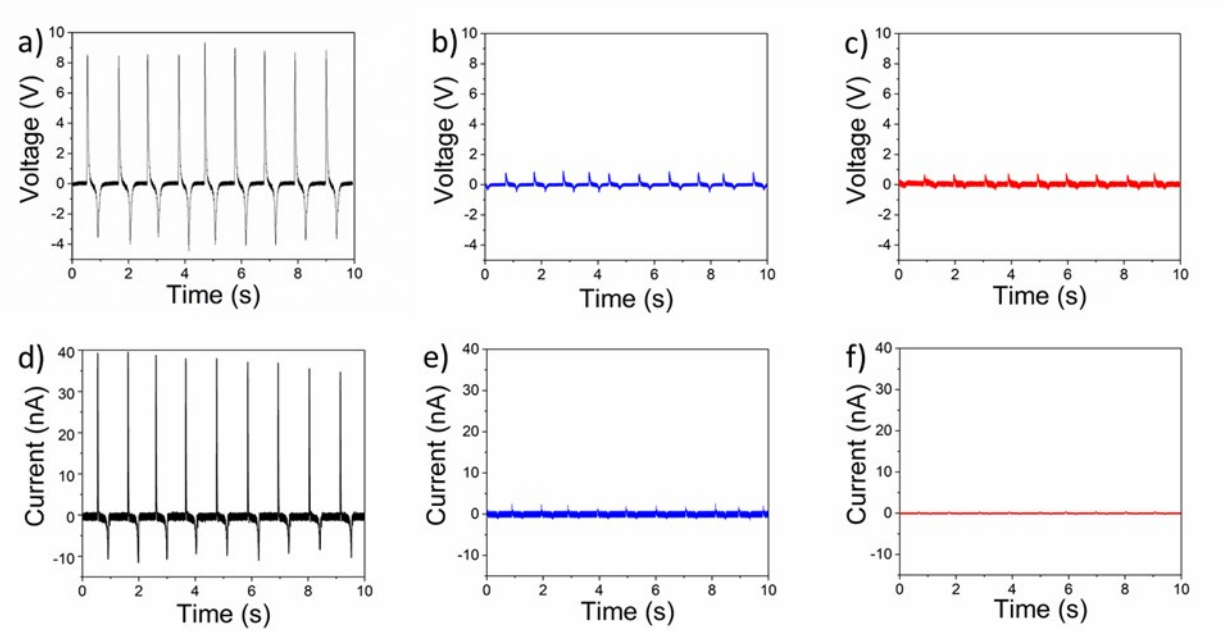

Figure S6. Open-circuit voltage (V_{OC}) generated by the TENG device based on EOC: (a) smooth vs porous films, (b) porous vs porous films, (c) smooth vs smooth films. Short-circuit current (I_{SC}) generated by the EOC-based TENG device: (d) smooth vs porous films, (e) porous vs porous films, (f) smooth vs smooth.

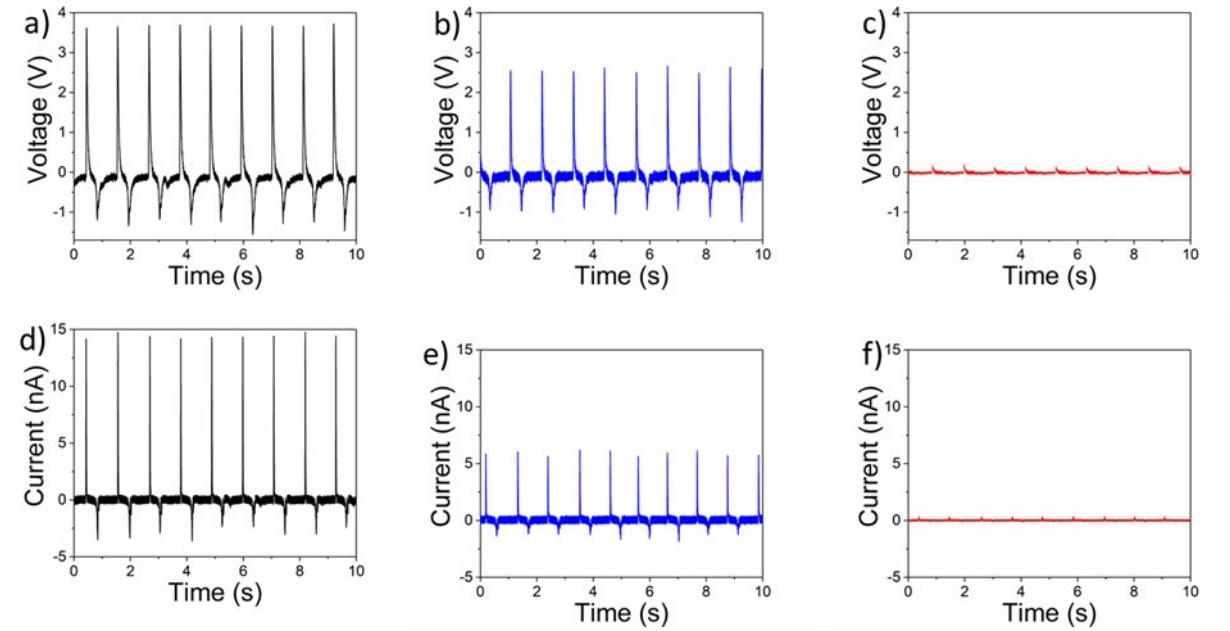

Figure S7. Open-circuit voltage (V_{OC}) generated by the TENG device based on PC: (a) smooth vs porous films, (b) porous vs porous films, (c) smooth vs smooth films. Short-circuit current (I_{SC}) generated by the PC-based TENG device: (d) smooth vs porous films, (e) porous vs porous films, (f) smooth vs smooth.

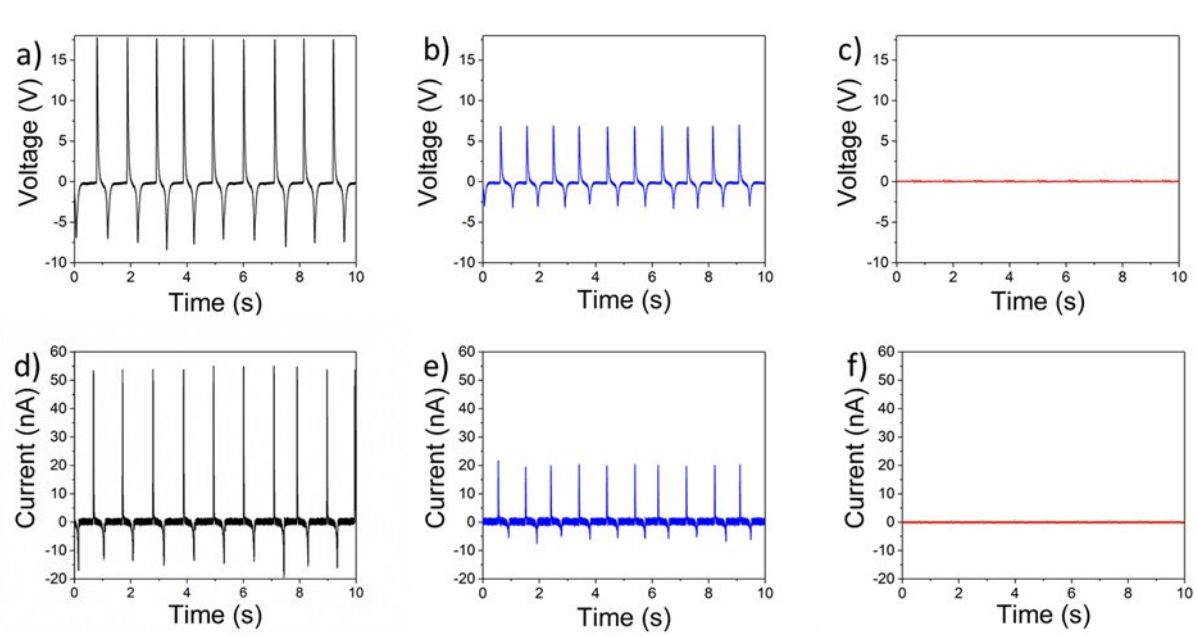

Figure S8. Open-circuit voltage (V_{OC}) generated by the TENG device based on PMMA: (a) smooth vs porous films, (b) porous vs porous films, (c) smooth vs smooth films. Short-circuit current (I_{SC}) generated by the PMMA-based TENG device: (d) smooth vs porous films, (e) porous vs porous films, (f) smooth vs smooth.

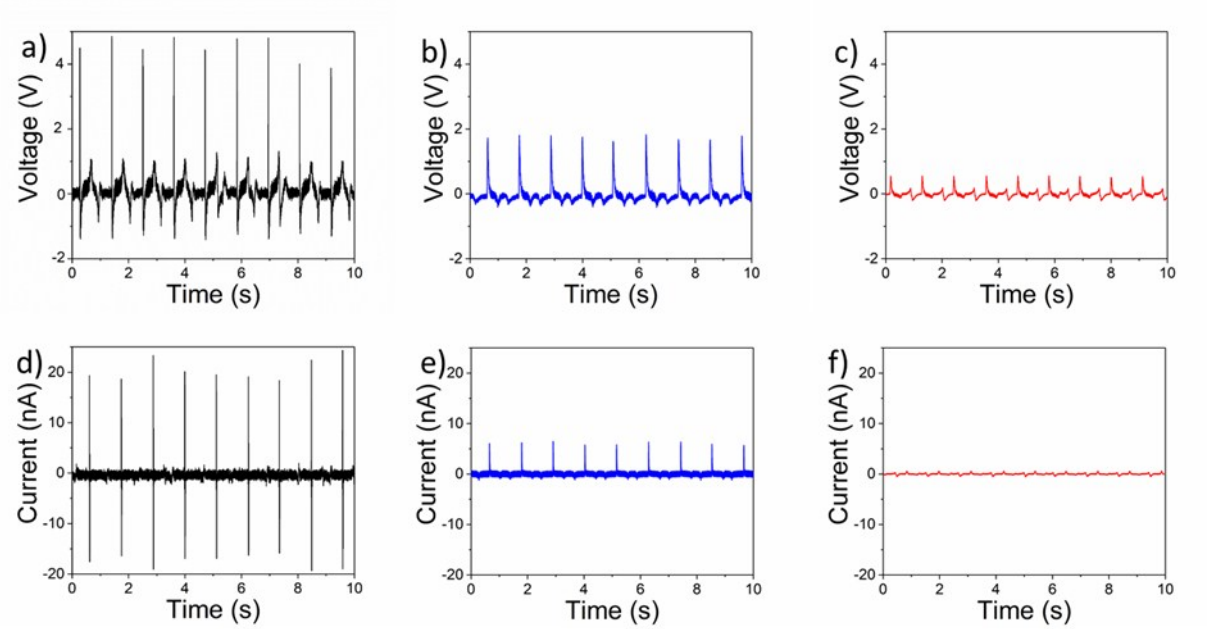

Figure S9. Open-circuit voltage (V_{OC}) generated by the TENG device based on PS (a) smooth vs porous films, (b) porous vs porous films, (c) smooth vs smooth films. Short-circuit current (I_{SC}) generated by the PS-based TENG device: (d) smooth vs porous films, (e) porous vs porous films, (f) smooth vs smooth.

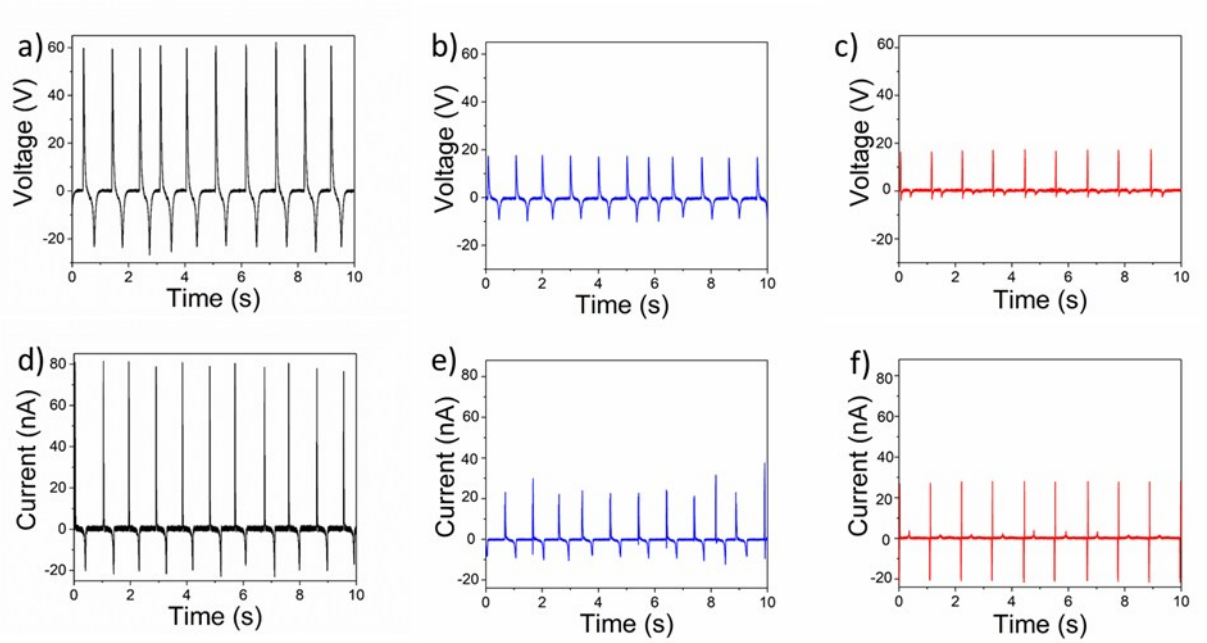

Figure S10. Open-circuit voltage (V_{OC}) generated by the TENG device based on SEBS (a) smooth vs porous films, (b) porous vs porous films, (c) smooth vs smooth films. Short-circuit current (I_{SC}) generated by the SEBS-based TENG device: (d) smooth vs porous films, (e) porous vs porous films, (f) smooth vs smooth.

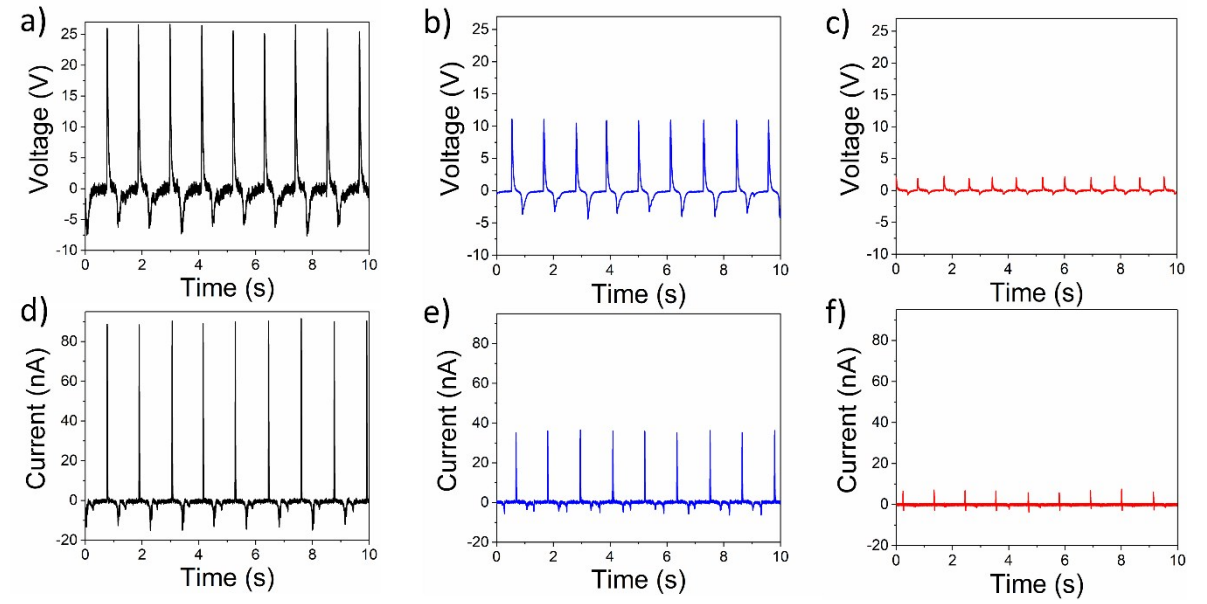

Figure S11. Open-circuit voltage (V_{OC}) generated by the TENG device based on PVDF (a) smooth vs porous films, (b) porous vs porous films, (c) smooth vs smooth films. Short-circuit current (I_{SC}) generated by the PVDF-based TENG device: (d) smooth vs porous films, (e) porous vs porous films, (f) smooth vs smooth.

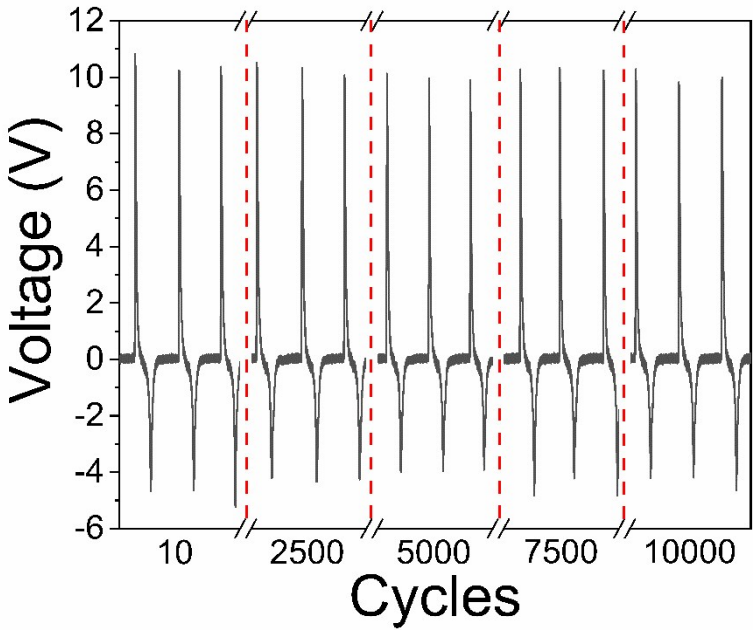

Figure S12. Long-term stability of TENG device based on EOC films during 10,000 contact-separation cycles.

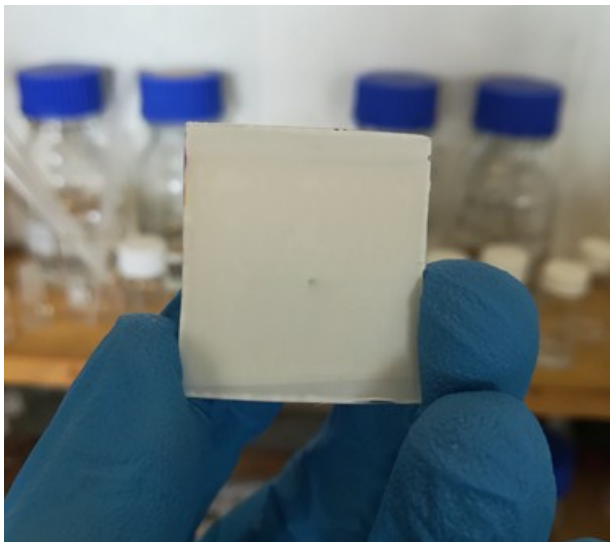

Figure S13. Photo of porous PVDF layer obtained through immersion-precipitation.

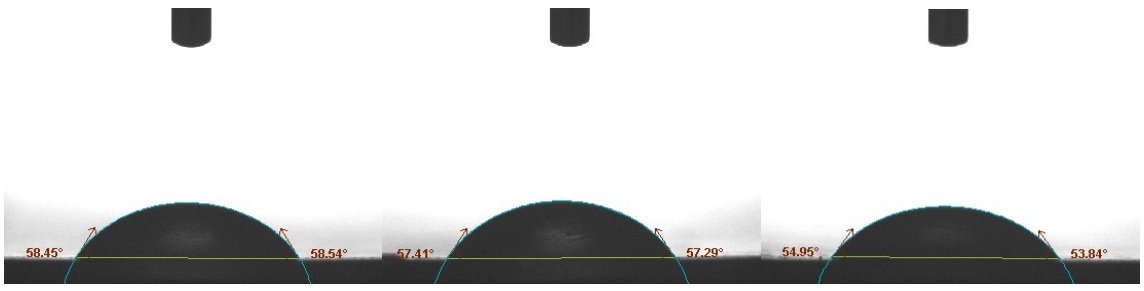

Figure S14. Water contact angle measurements on smooth PVDF films.

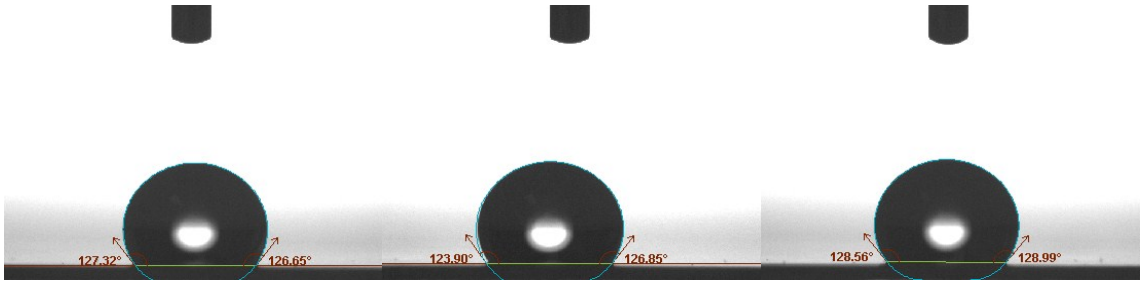

Figure S15. Water contact angle measurements on porous PVDF films.

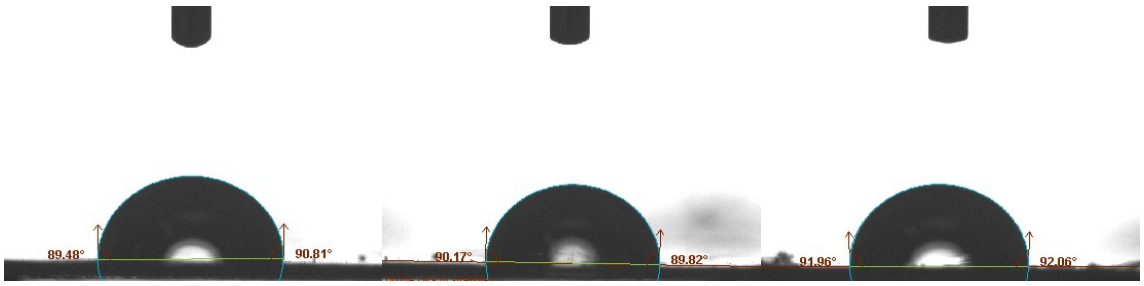

Figure S16. Water contact angle measurements on smooth PC films.

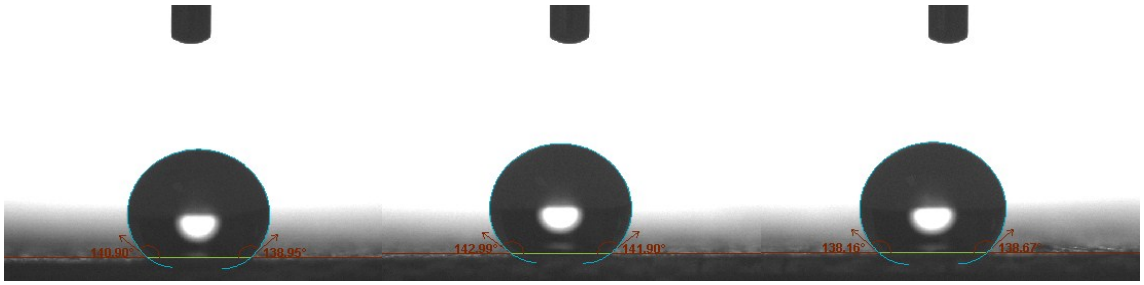

Figure S17. Water contact angle measurements on porous PC films.

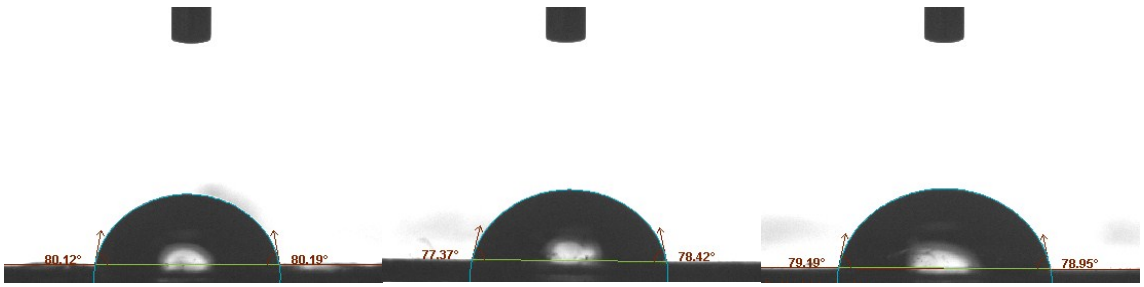

Figure S18. Water contact angle measurements on smooth EC films.

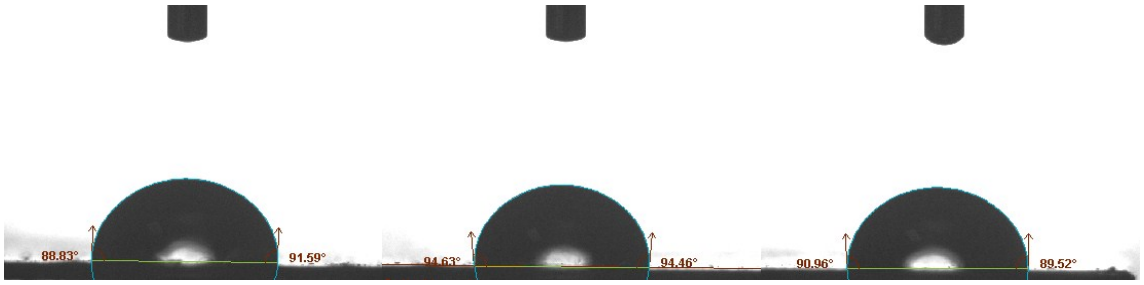

Figure S19. Water contact angle measurements on porous EC films.

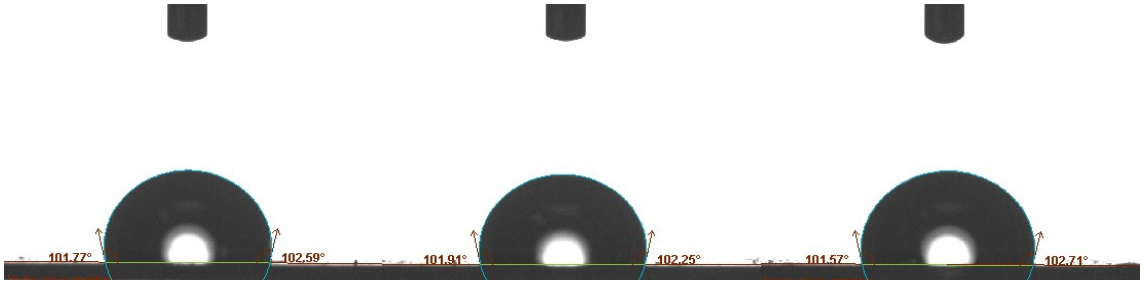

Figure S20. Water contact angle measurements on smooth PS films.

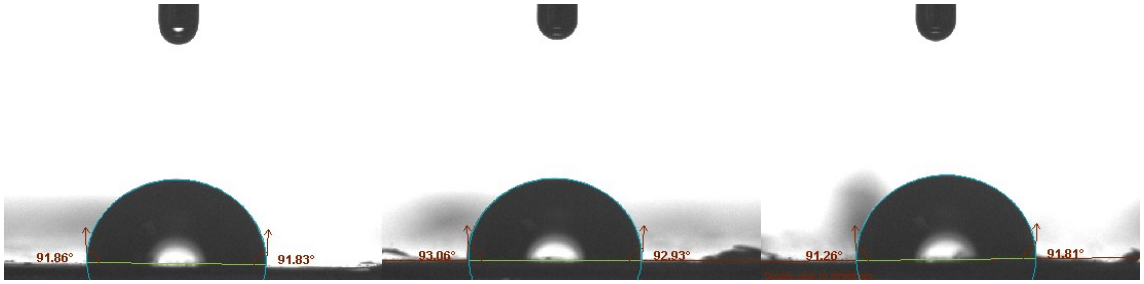

Figure S21. Water contact angle measurements on porous PS films.

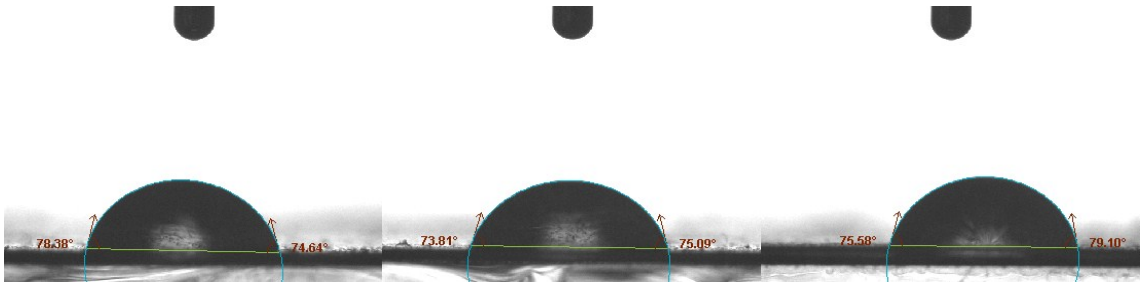

Figure S22. Water contact angle measurements on smooth EOC films.

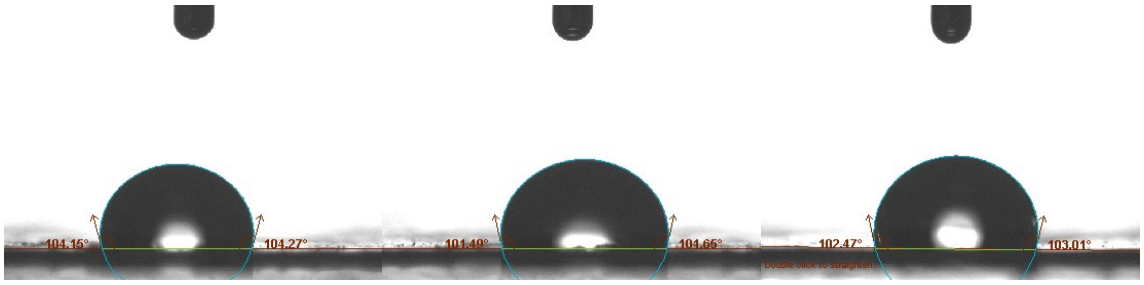

Figure S23. Water contact angle measurements on porous EOC films.

Figure S24. Water contact angle measurements on smooth PMMA films.

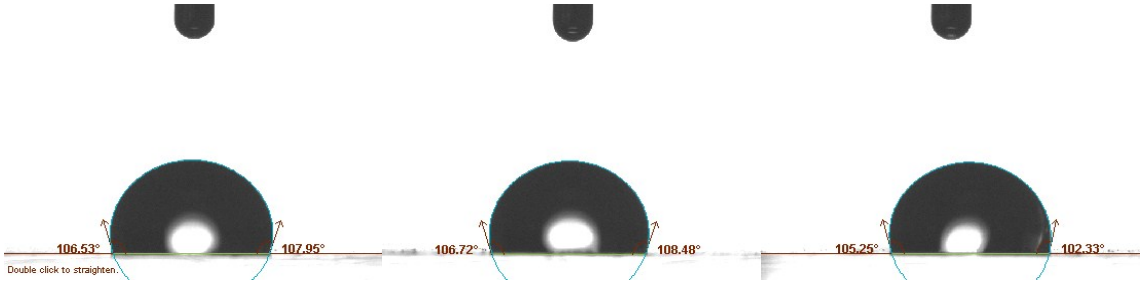

Figure S25. Water contact angle measurements on porous PMMA films.

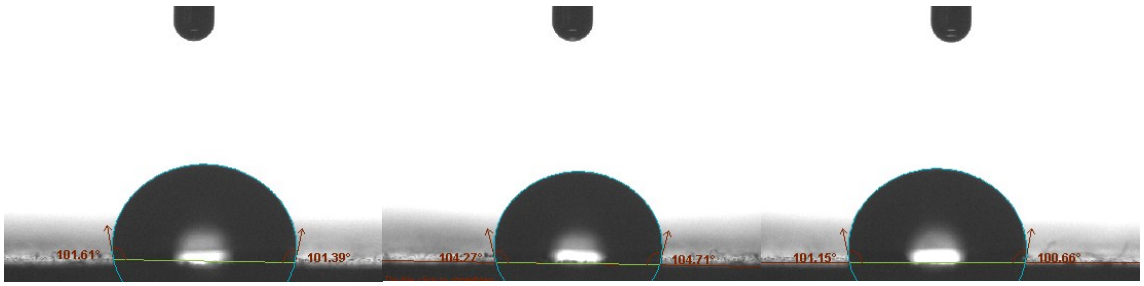

Figure S26. Water contact angle measurements on smooth SEBS films.

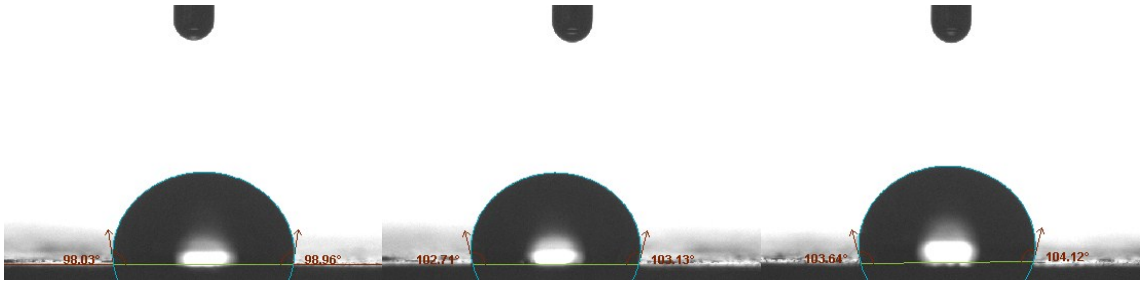

Figure S27. Water contact angle measurements on porous SEBS films.

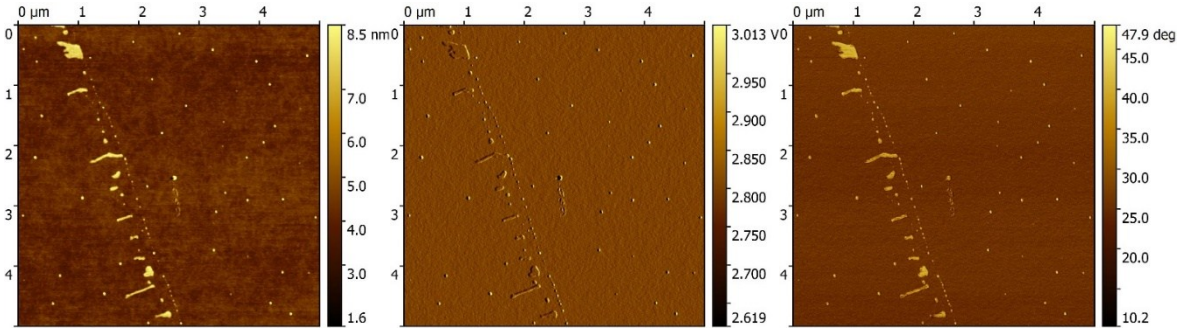

Figure S28. Surface topography, tapping amplitude and tapping phase images measured by AFM for a smooth PC sample.

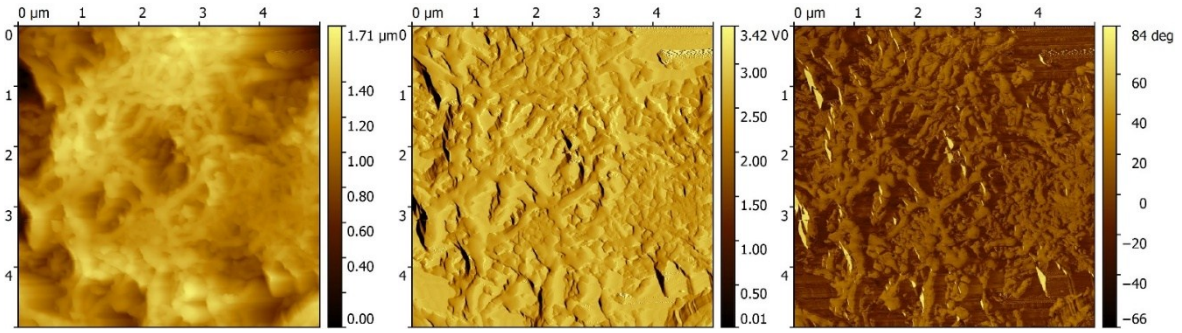

Figure S29. Surface topography, tapping amplitude and tapping phase images measured by AFM for a porous PC sample.

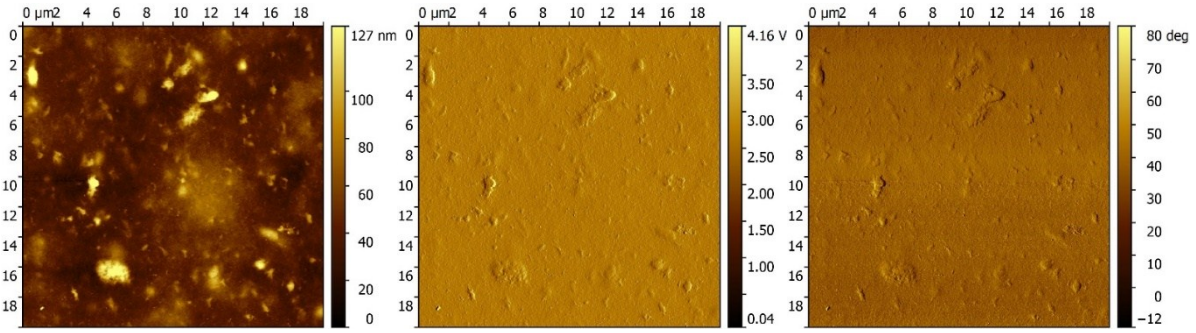

Figure S30. Surface topography, tapping amplitude and tapping phase images measured by AFM for a smooth EC sample.

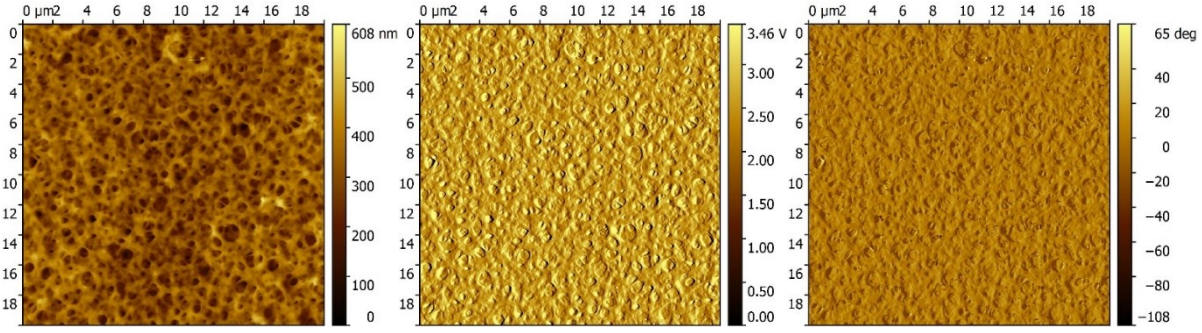

Figure S31. Surface topography, tapping amplitude and tapping phase images measured by AFM for a porous EC sample.

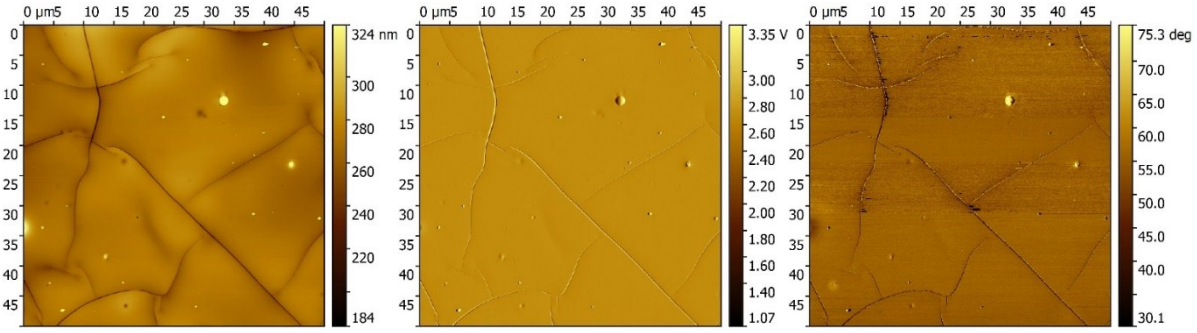

Figure S32. Surface topography, tapping amplitude and tapping phase images measured by AFM for a smooth PS sample.

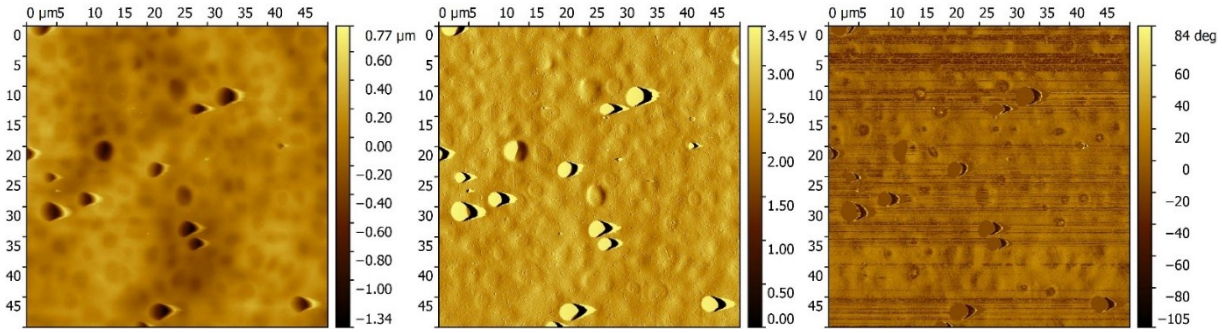

Figure S33. Surface topography, tapping amplitude and tapping phase images measured by AFM for a porous PS sample.

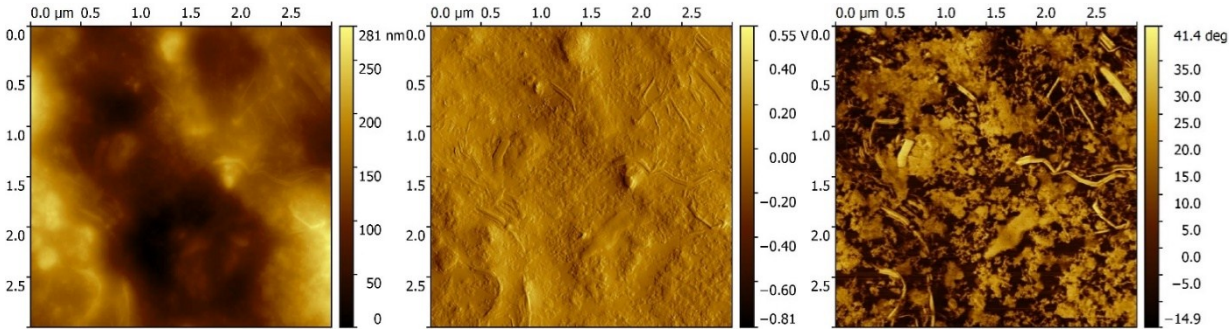

Figure S34. Surface topography, tapping amplitude and tapping phase images measured by AFM for a smooth SEBS sample.

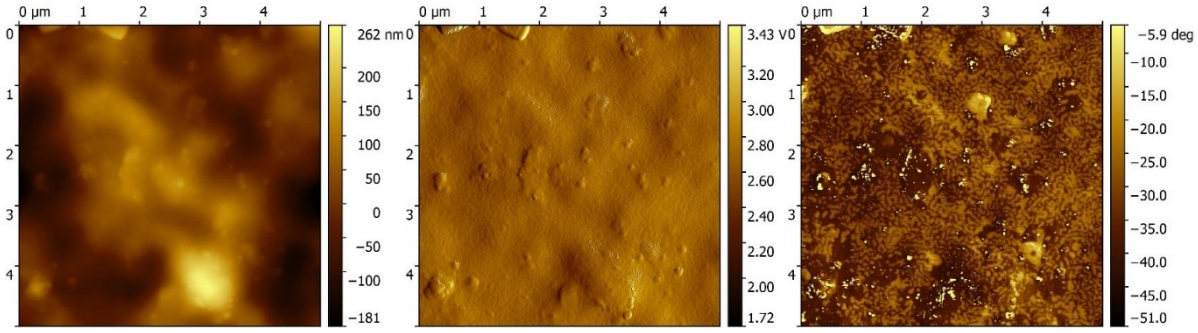

Figure S35. Surface topography, tapping amplitude and tapping phase images measured by AFM for a porous SEBS sample.

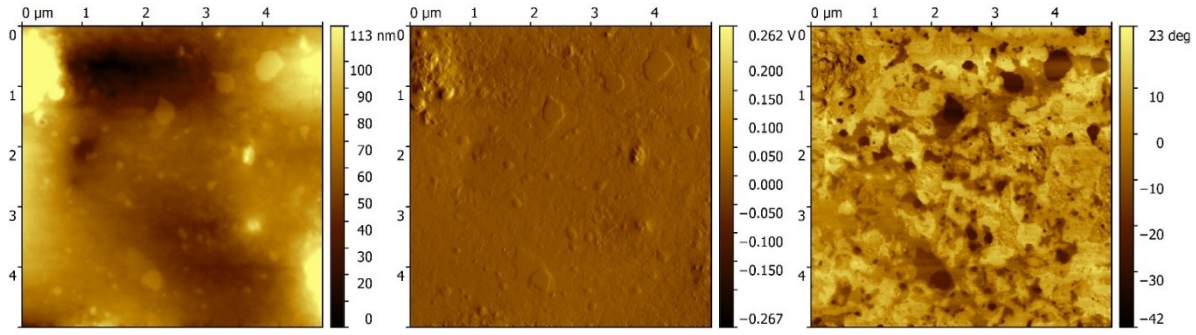

Figure S36. Surface topography, tapping amplitude and tapping phase images measured by AFM for a smooth EOC sample.

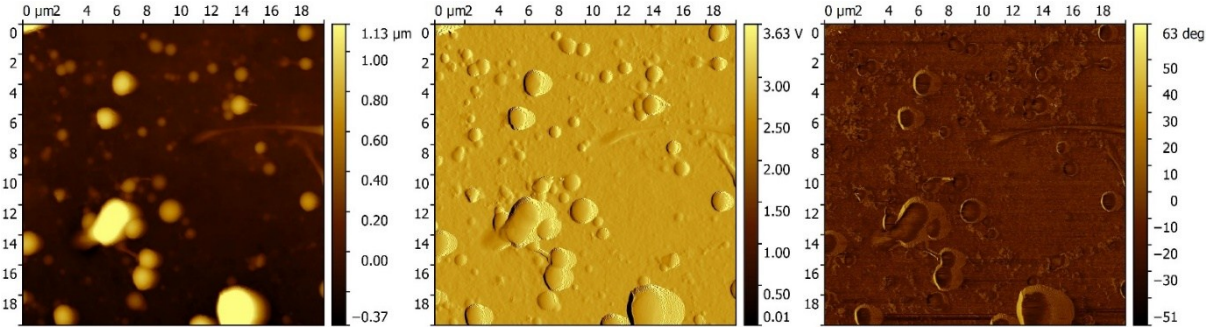

Figure S37. Surface topography, tapping amplitude and tapping phase images measured by AFM for a porous EOC sample.

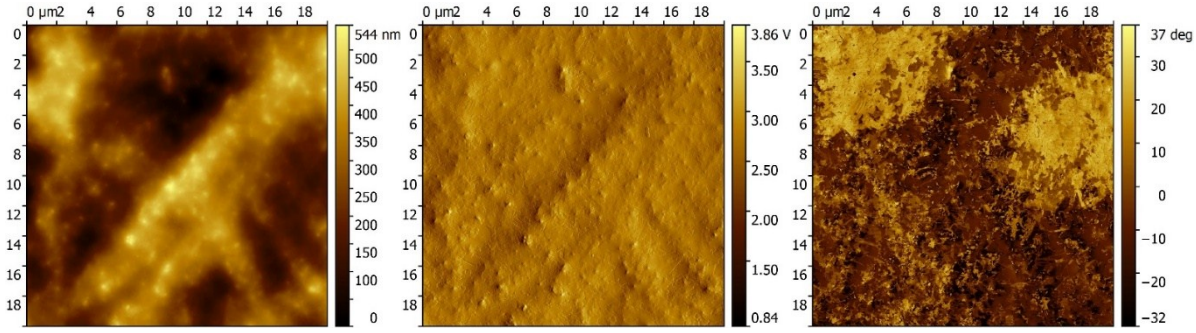

Figure S38. Surface topography, tapping amplitude and tapping phase images measured by AFM for a smooth PVDF sample.

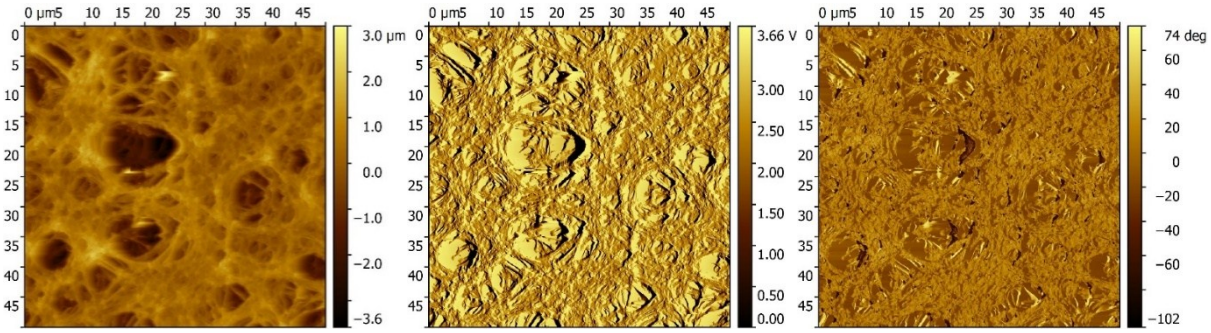

Figure S39. Surface topography, tapping amplitude and tapping phase images measured by AFM for a porous PVDF sample.

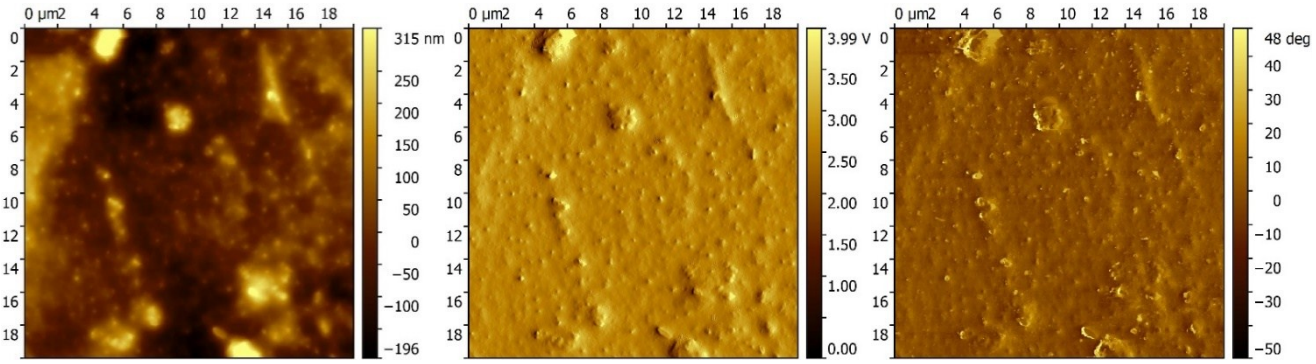

Figure S40. Surface topography, tapping amplitude and tapping phase images measured by AFM for a smooth PMMA sample.

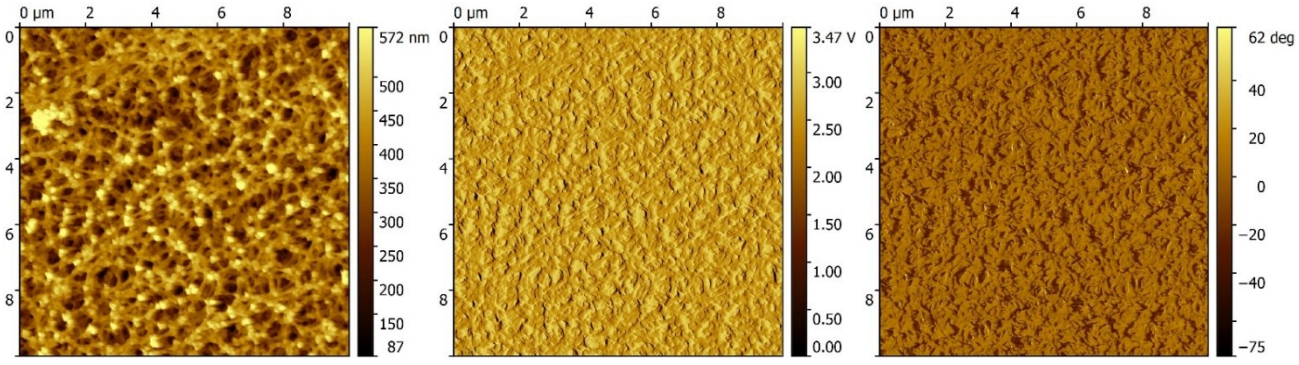

Figure S41. Surface topography, tapping amplitude and tapping phase images measured by AFM for a porous PMMA sample.

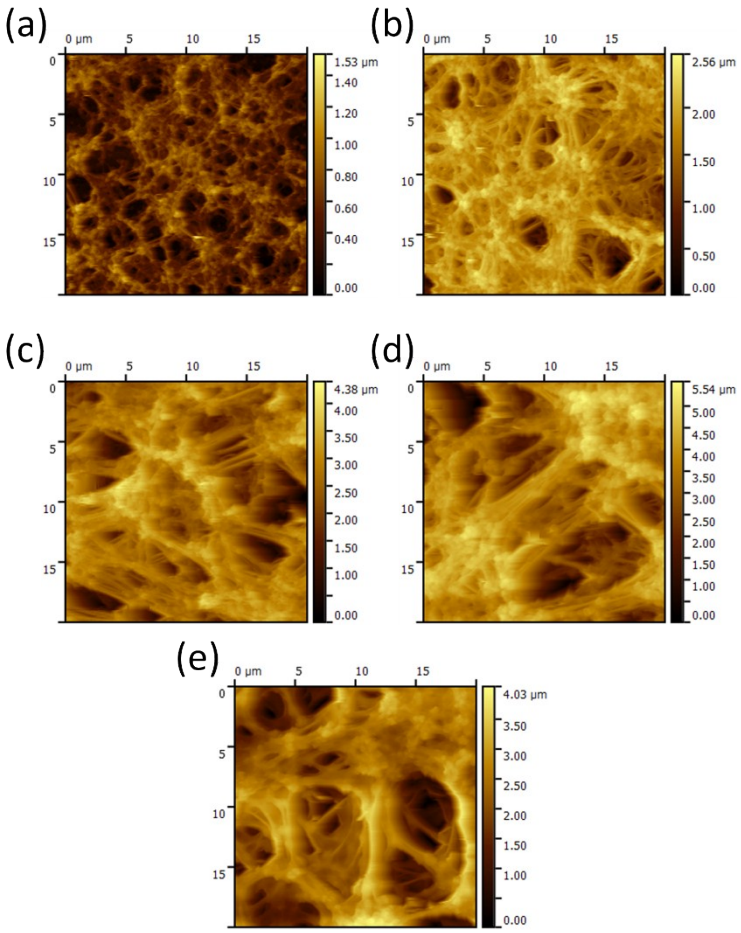

Figure S42. AFM images showing height profile of PVDF film surfaces prepared from (a) 5, (b) 10, (c) 15, (d) 20 and (e) 25 wt% solutions by immersion precipitation.

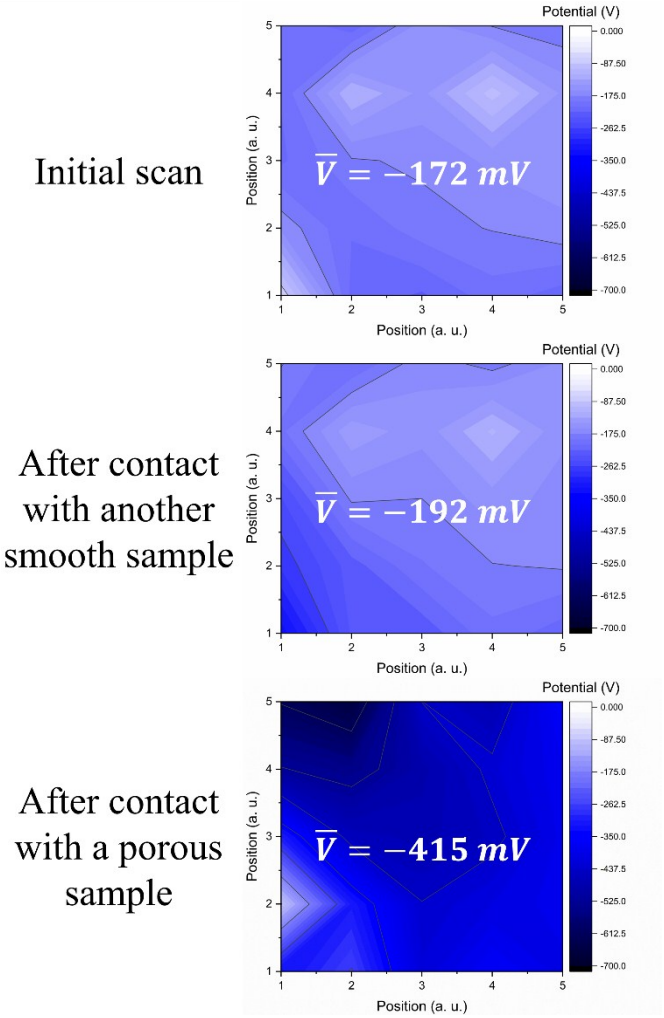

Figure S43. Scanning Kelvin probe measurements of smooth PVDF sample.

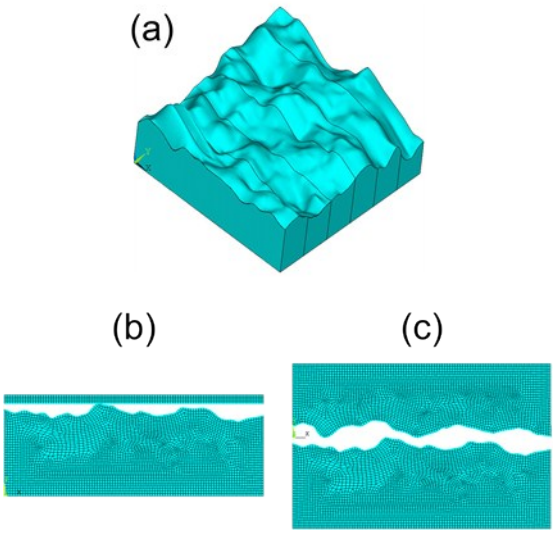

Figure S44. (a) PVDF surface 3D image from AFM measurement. Schematics of (b) smooth vs rough, and (c) rough vs rough PVDF contact cases.

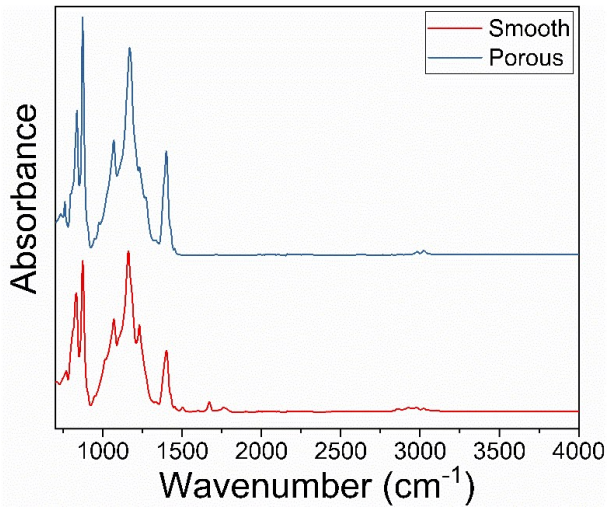

Figure S45. ATR-FTIR absorbance spectra for smooth and porous PVDF samples.

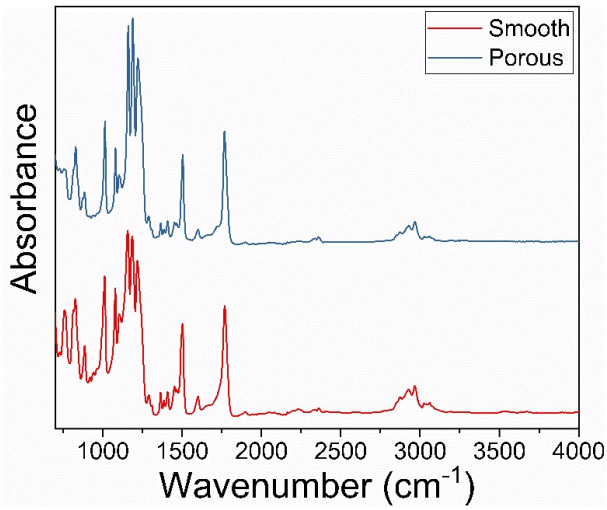

Figure S46. ATR-FTIR absorbance spectra for smooth and porous PC samples.

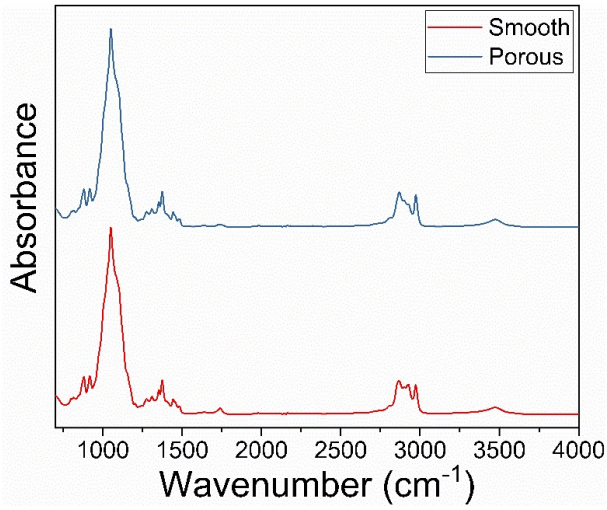

Figure S47. ATR-FTIR absorbance spectra for smooth and porous EC samples.

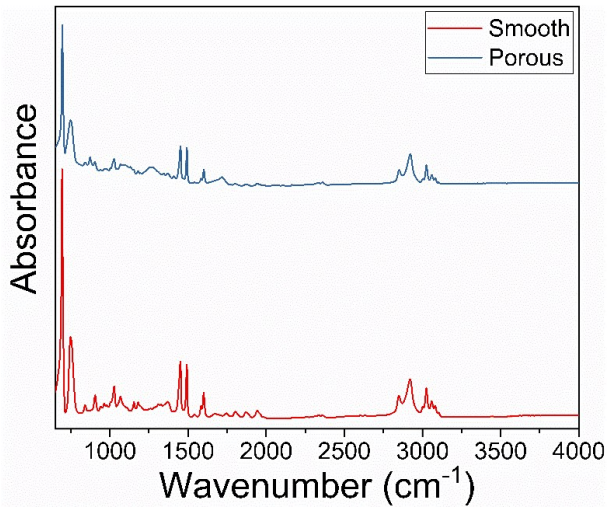

Figure S48. ATR-FTIR absorbance spectra for smooth and porous PS samples.

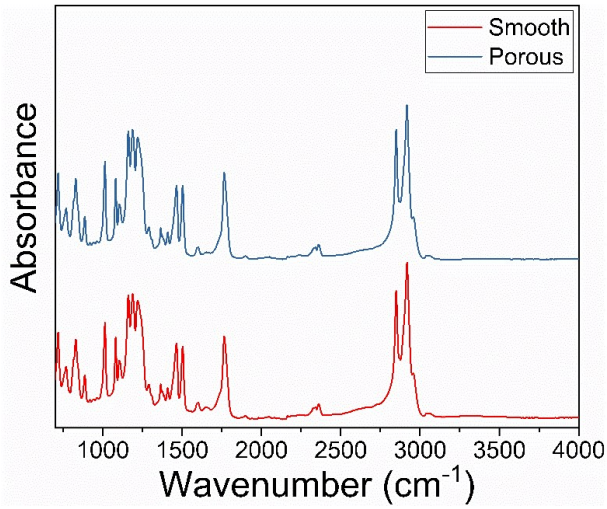

Figure S49. ATR-FTIR absorbance spectra for smooth and porous EOC samples.

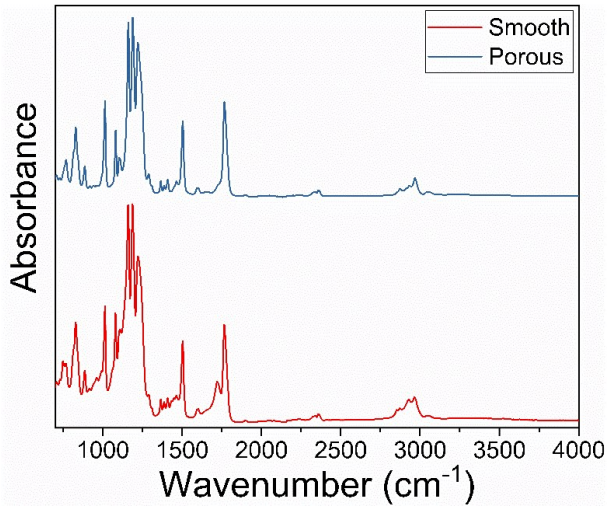

Figure S50. ATR-FTIR absorbance spectra for smooth and porous PMMA samples.

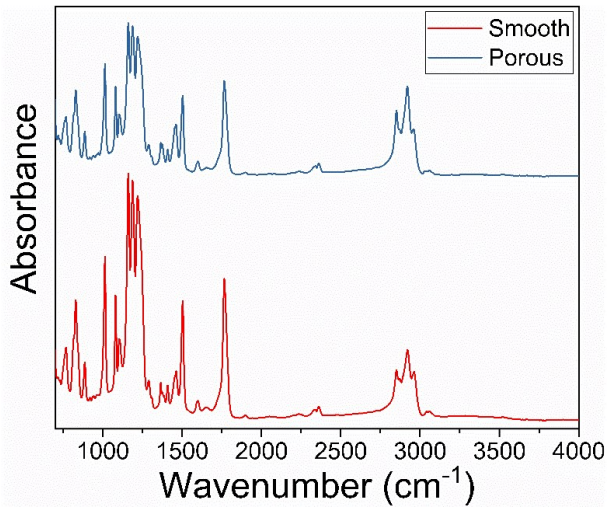

Figure S51. ATR-FTIR absorbance spectra for smooth and porous SEBS samples.

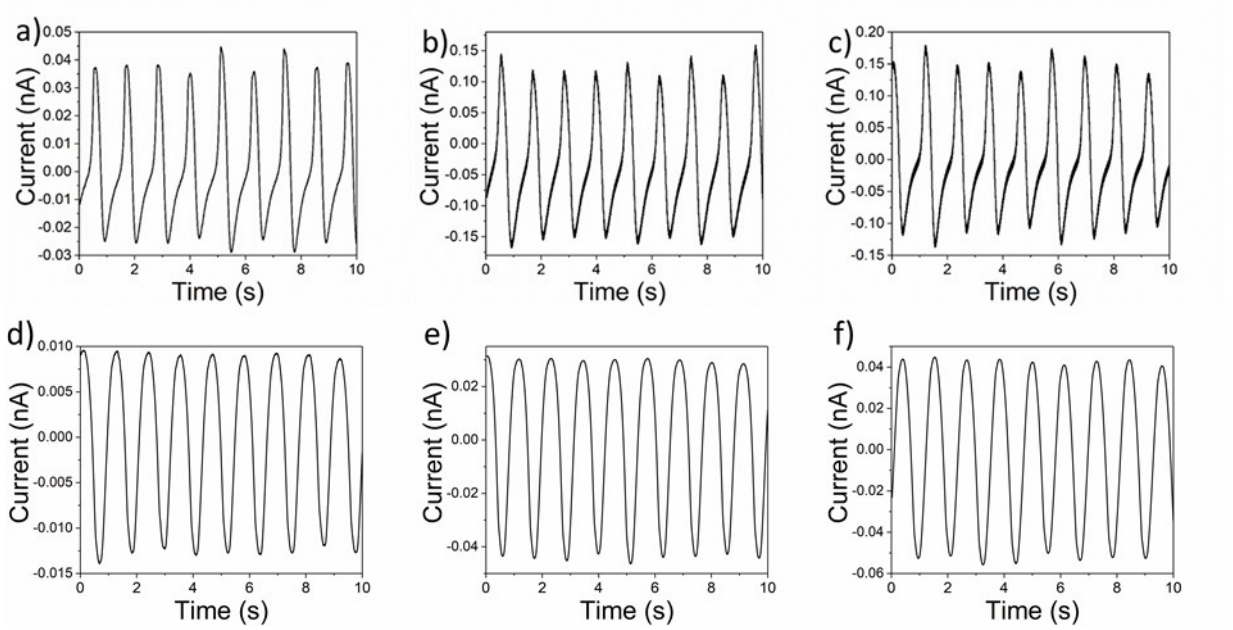

Figure S52. Short-circuit current (I_{SC}) generated in the piezo regime when loading and unloading contacted PVDF membranes with different pore size without separation: (a) 0.10 µm vs 0.22 µm, (b) 0.22 µm vs 0.45 µm, (c) 0.10 µm vs 0.45 µm, (d) 0.10 µm vs 0.10 µm, (e) 0.22 µm vs 0.22 µm and (f) 0.45 µm vs 0.45 µm.

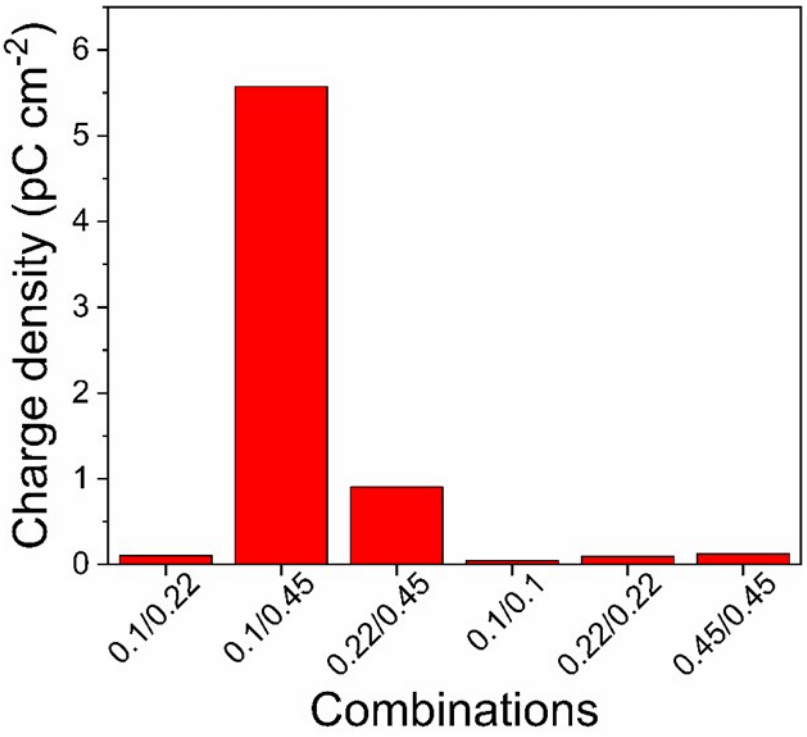

Figure S53. Charge density calculated from current measured in the piezo regime between PVDF membranes with different porosity: 0.10 µm vs 0.22 µm, 0.10 µm vs 0.45 µm, 0.22 µm vs 0.45 µm, 0.10 µm vs 0.10 µm, 0.22 µm vs 0.22 µm and 0.45 µm vs 0.45 µm.

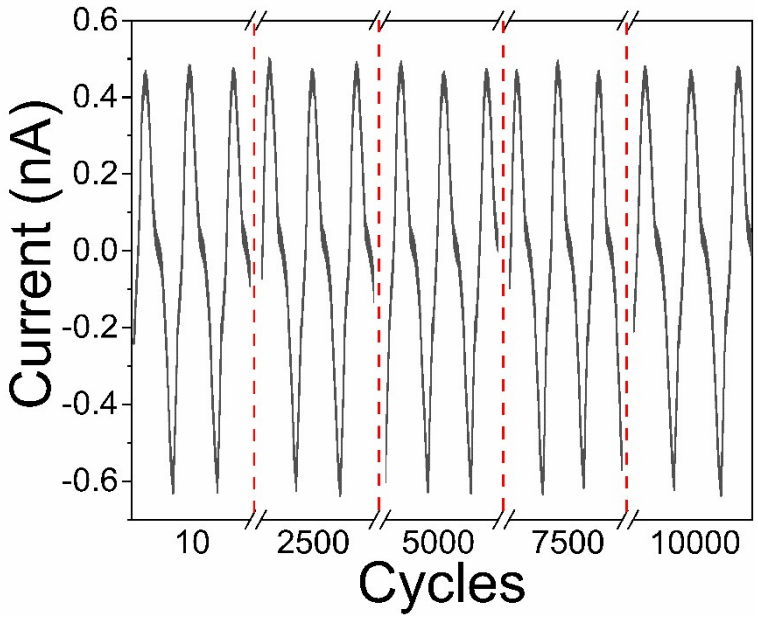

Figure S54. Long-term stability of multi-layered membrane, with 0.10/0.45/0.22 µm stacking order during 10,000 compression cycles.

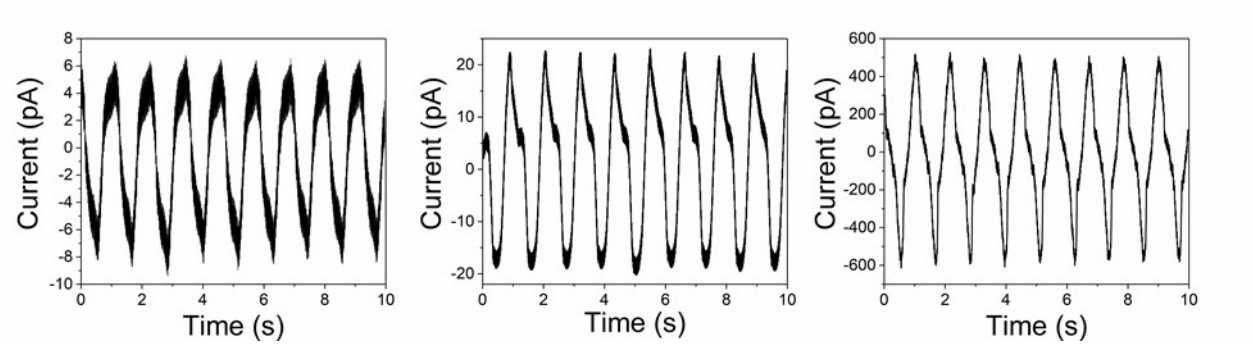

Figure S55. Short-circuit current (I_{SC}) generated by multi-layered membrane, with 0.10/0.45/0.22 μm stacking order, in the piezo-regime at different loading: 10 N (left), 50 N (middle) and 100 N (right).

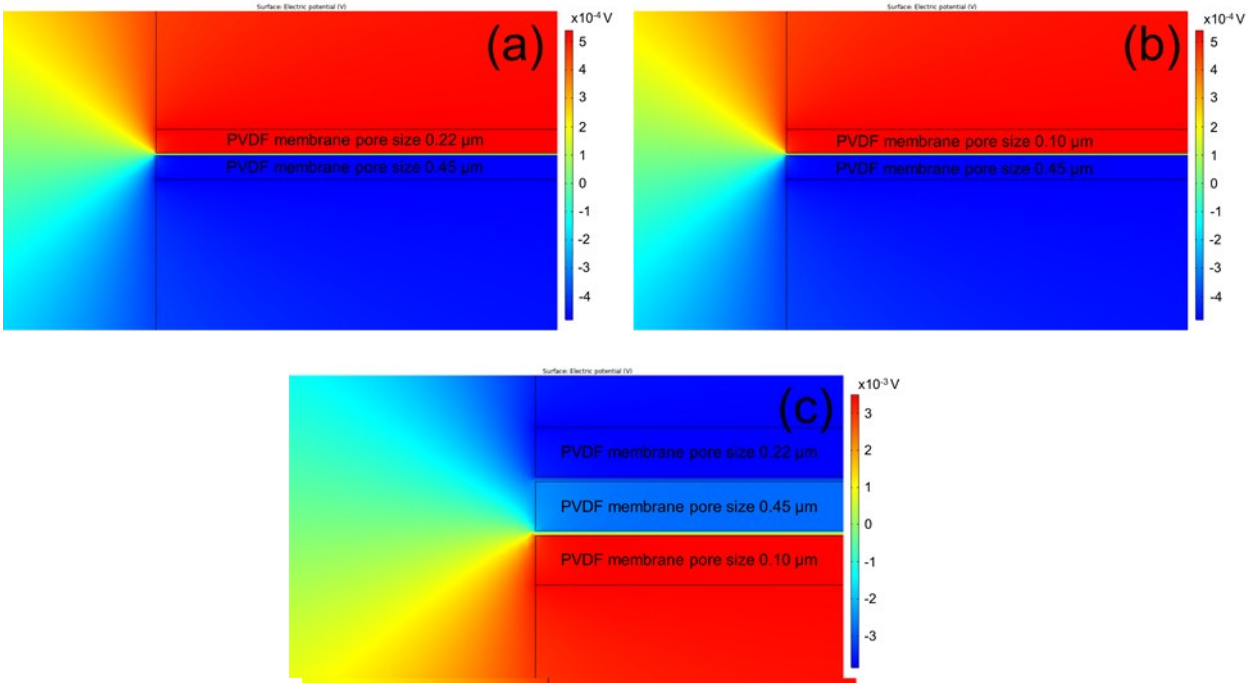

Figure S56. Simulated electric potential for 3 cases: (a) potential arising from the contacting interface between PVDF membranes with pore size 0.22 μm and 0.45 μm, (b) potential arising from the contacting interface between PVDF membranes with pore size 0.10 μm and 0.45 μm and (c) potential arising from the two contacting interfaces, with PVDF membrane with pore size 0.45 μm in the middle and membranes with pore sizes 0.10 μm and 0.22 μm on the outside. The electric potential was simulated with COMSOL finite element analysis software. The charge density used for simulations was calculated from measured current in the piezo regime.

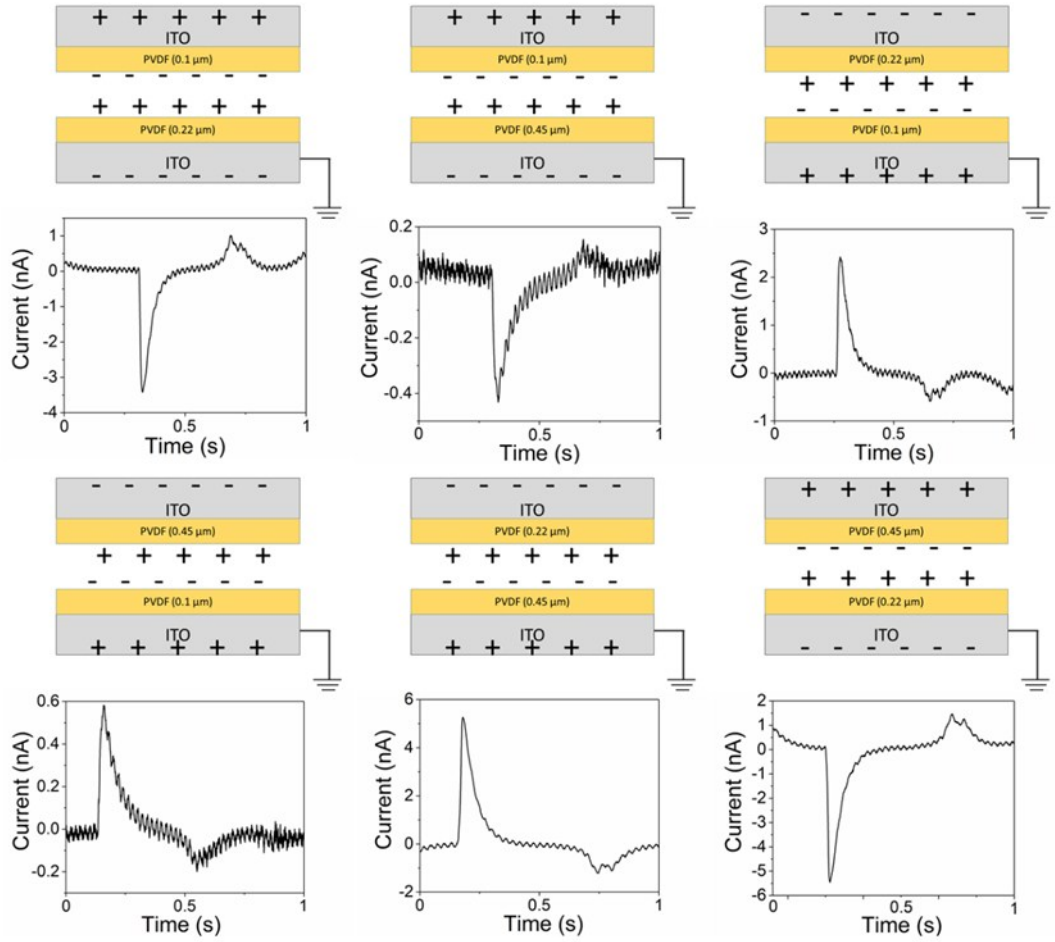

Figure S57. Net surface charge on combinations of varying porosity PVDF membranes. The membranes were adhered to grounded ITO. Short-circuit current (I_{SC}) pulses were recorded between the ground and ITO plate by a custom-made voltage divider connected to an electrometer and oscilloscope to provide high time resolution.

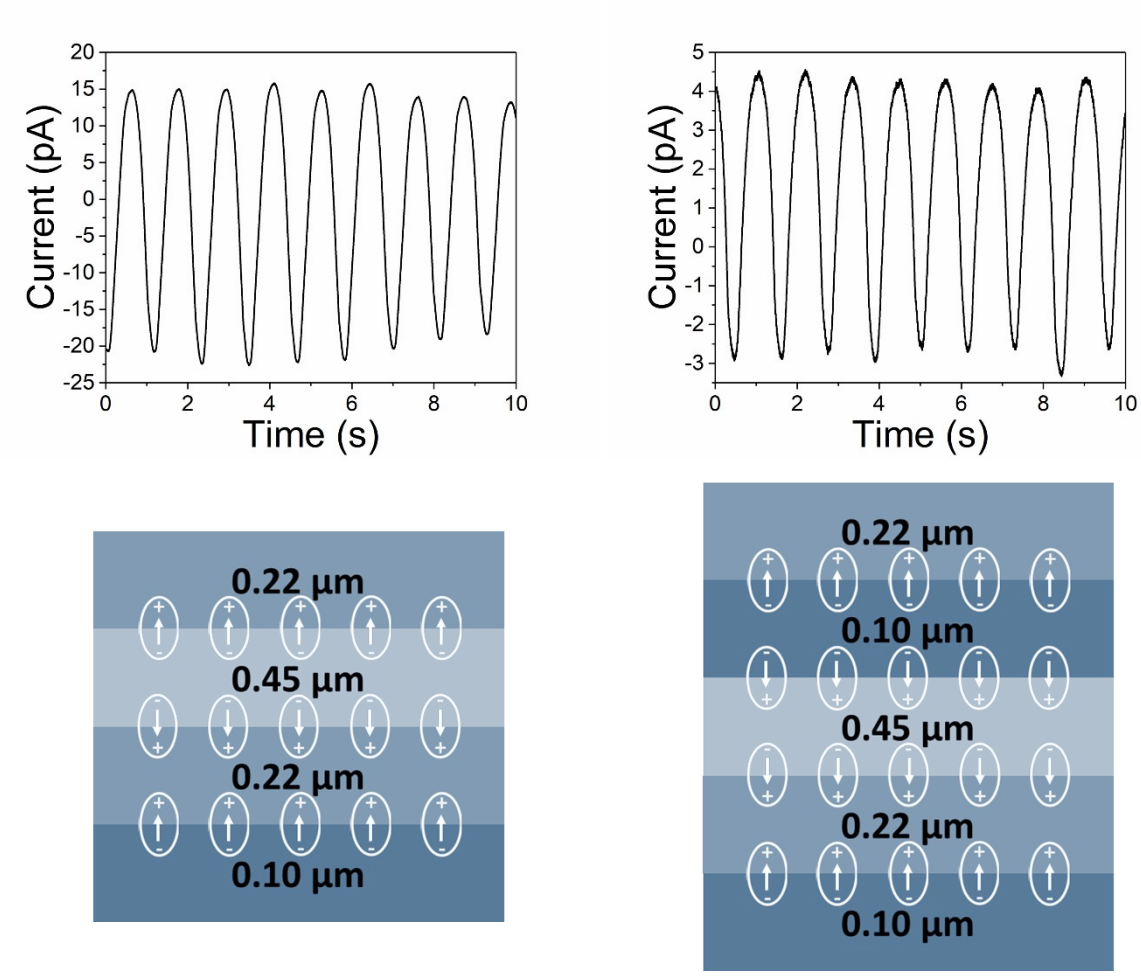

Figure S58. Short-circuit current (I_{SC}) measured in the piezo-regime under a 100 N load for four (top left) and five (top right) multi-layered membranes, along with a schematic of the inverse dipole formation (bottom). The sign of the charge formed on each membrane surface at the interface was measured experimentally (Figure S18).

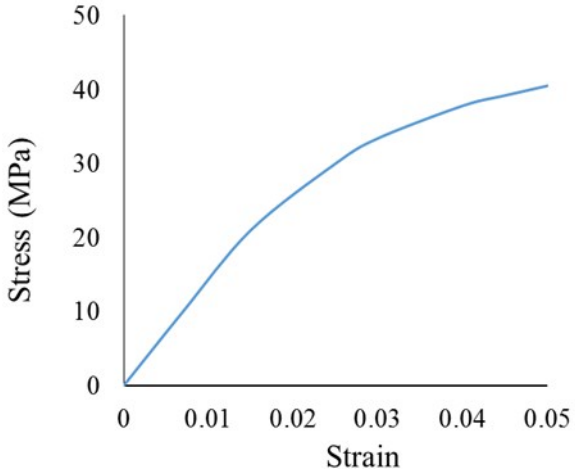

Figure S59. Experimentally measured stress-strain behavior of PVDF used in TENG devices.

Table S1. Polymer surface charge density.

Polymer	Porous vs smooth [pC cm^{-2}]	Porous vs porous [pC cm^{-2}]	Smooth vs smooth [pC cm^{-2}]
EC	30.51	11.41	2.08
EOC	115.79	5.76	2.17
PC	41.39	18.45	1.44
PMMA	168.90	67.40	1.13
PS	18.37	15.79	5.42
SEBS	246.36	144.65	10.40

Table S2. Contact angle measurement performed on seven different polymers with smooth or porous surface. Three parallel time-dependant contact angle measurements were performed on each polymer sample.

Polymer	Contact angle, °					
	Smooth			Porous		
	1.	2.	3.	1.	2.	3.
PVDF	58.8±0.2	56.8±1.9	53.4±2.4	127.2±0.8	126.9±0.5	128.9±0.3
PC	89.8±0.4	90.2±1.0	92.8±1.4	140.0±0.1	142.6±0.2	138.6±0.3
EC	81.5±3.6	77.8±1.0	79.2±0.1	90.0±2.0	94.7±0.2	90.1±0.2
PS	102.5±0.4	103.2±2.0	102.6±0.9	91.5±0.3	93.0±0.2	90.9±0.5
EOC	76.0±1.0	73.3±3.4	77.9±1.3	104.3±0.5	102.7±0.8	103.4±0.9
PMMA	39.2±3.3	42.0±3.3	49.6±2.5	107.0±1.0	107.4±0.3	103,8±0.3
SEBS	101.5±1.5	105.2±0.9	102.2±1.2	102.5±6.6	102.3±0.5	102.6±1.3

Table S3. Statistical results of polymer RMS surface roughness measurements by AFM. Additionally, scan areas used for determination of roughness are listed.

Polymer	Smooth [nm]	Porous [nm]	Scan areas [μm]
EC	21.21 ± 11.45	143 ± 127	20×20 and 50×50
EOC	112 ± 88	297 ± 59	50×50
PC	1.09 ± 0.48 nm	406 † ‡	10×10 and 20×20
PMMA	75.26 ± 28.83	74.2 ± 16.06 ‡	10×10, 20×20 and 50×50
PS	8.19 ± 1.97	168 ± 7	20×20 and 50×50
SEBS	267 ± 170	202 ± 117 ‡	50×50
PVDF	135 ± 48	579 ± 206	20×20 and 50×50

† Insufficient number of successful scans to calculate deviation.
‡ Estimated from measurements with lowest roughness values as measurements with too large surface feature height difference were excluded due to restrictions imposed by AFM z-direction actuation limit.

Table S4. Surface roughness (RMS) measured by AFM for PVDF films obtained from varying concentration solutions.

PVDF [wt%]	Roughness [nm]
5	174-235
10	302-347
15	541-593
20	753-878
25	919-1000

Supplementary Discussion S1

We have performed additional AFM phase measurements. Generally, the scan area required for correct surface roughness measurement depends on the type of sample. For smooth and homogeneous samples with small surface roughness, small scan areas (5x5 or 10x10 μm) provide sufficient information for correct surface roughness evaluation. The obtained surface roughness value increases with increasing scan area and approaches plateau at specific scan range. This is expected because increasing scan area includes more and more surface features. For example, it is sufficient to use scan area of 10x10 μm for a porous PMMA as the scan area of 20x20 μm does not result in further increase in the obtained RMS surface roughness value. However, for most samples the obtained surface roughness value reaches a constant value in the scan area ranging between 20x20 and 50x50 μm, thus requiring scan area of 50x50 μm. AFM images were recorded from each sample at different scan ranges to take this effect into account. The root mean squared (RMS) surface roughness was measured from at least three different areas on every film, and the RMS surface roughness uncertainty was calculated statistically at a 95% confidence level. Additionally, for some samples small scan area (3x3 or 5x5 μm) was used to obtain images to show surface features at suitable scale for tapping phase and surface topography analysis. For 50x50 μm images scan rate of 0.1 Hz was used in case of rough samples and 0.2 Hz for some smooth samples. For smaller scan areas scan rate of 0.3 Hz was used.

For each sample height sensor (surface topography), tapping amplitude and tapping phase images were recorded. Set-point amplitude as well as PID parameters were extensively and meticulously varied in order to determine whether tapping phase images reveal features beyond direct correlation with surface topography images. Light, moderate and hard tapping modes have been shown to reveal microlayer patterns in polyethylene which is absent in topography images [DOI: 10.1016/S0039-6028(96)01591-9]. It is well known that tapping phase images are mostly influenced by surface topography. A shadowing in scan direction occurs at areas where large changes are present in the topography [DOI: 10.1016/S0006-3495(01)76266-2]. Similarly, a tilted sample due to uneven substrate or gradient in film thickness makes it harder to interpret tapping phase images. The phase image is often ignored as chemical and morphological-dependent parts are not well distinguished in the tapping phase AFM images [DOI: 10.1111/j.1365-2818.2009.03282.x]. Nevertheless, phase imaging atomic force microscopy is considered as a powerful tool for material's surface characterization as it is known that phase contrast arises from differences in the energy dissipation between the tip and the sample [DOI: 10.1063/1.120039 and DOI: 10.1063/1.122632]. The energy dissipation between the tip and the sample in turn depends on the sample stiffness. Therefore, phase imaging can provide a map of stiffness variation on the sample surface and a stiffer region exhibits more positive phase shift and appears brighter in a phase image [DOI: 10.1016/S0039-6028(96)01591-9].

For very rough samples (porous PC, porous EC, porous PVDF and porous PMMA) the tapping phase images contain no useful information and as expected significant shadowing dominates the tapping phase images. However, despite the lack of severe shadowing effects in smooth EC, porous EOC, smooth PMMA, and both smooth and porous PS the tapping phase images reveal no contrast beyond obvious influences from surface topography. It can be expected in single-polymer films with no additives. No crystalline phases are also detected in these samples. Tapping phase image of smooth PC shows good correlation with surface topography where some higher spots cover the smooth polymer surface. These surface features may exhibit higher stiffness but since these spots are higher, AFM as method remains inconclusive in this regard. Also, no comparison with porous PC is possible due to the high roughness.

Tapping phase images of smooth and porous SEBS show clear and interesting contrast not visible in topography images. Smooth SEBS seems to contain crystalline areas with higher stiffness which are only partially visible on topography images, covering roughly half of the area. Porous SEBS on the other hand seems to exhibit fine phase separated structure with significantly different distribution and with overall lower stiffness. These images also confirm that our measurements can successfully extract useful information from tapping phase imaging in case the sample properties are such that the basis for such contrast inherently exists in the sample. Smooth PVDF shows the clearest contrast in tapping phase images that is not visible on corresponding topography image. The areas of about 10 μm in diameter with different mechanical properties from the rest of the surface are clearly shown. It is important to note that such structures were observed on all images across the sample. Unfortunately, no tapping phase image comparison is possible with the corresponding porous PVDF due to high surface roughness.

In conclusion, tapping phase images were found not to provide useful information in general, mostly due to high roughness of large share of the samples. Thus, no comparison is possible with smoother samples in most cases. Obtaining topography images of such extreme samples in itself probes the limit of AFM method, so to obtain meaningful tapping phase images is even further out of reach for these samples.